



OPEN A wideband slot antenna for RF energy harvesting

Usman Yau¹, Jun Jiat Tiang¹, Surajo Muhammad², Nazih Khaddaj Mallat³ & Amjad Iqbal⁴

This study details the design, simulation, and experimental evaluation of a compact wideband slot antenna tailored for ambient radio frequency energy harvesting (RFEH) applications. The design incorporates an inverted T-shaped stub along with dual E-shaped stubs embedded within a rectangular slot, excited by an extended T-shaped microstrip feed line. The antenna, fabricated on an FR-4 substrate with a relative permittivity of 4.4, exhibits simulated and measured impedance bandwidth (BW) of 1.10 GHz and 1.05 GHz ranging from 0.87 to 1.97 GHz and 0.84 to 1.89 GHz both defined at the -10 dB respectively. It attains a peak realized gain of simulated (measured) 4.97 dBi (4.86 dBi), all within a compact footprint of $0.59\lambda_g \times 0.44\lambda_g$. Parametric analysis and comparative simulations were conducted to validate the effectiveness of the proposed design. Measurements obtained from experiments carried out in an anechoic chamber show a high level of consistency with the simulated data, reinforcing the accuracy and reliability of the simulation model. Integrating the antenna with a high-efficiency rectifier circuit results in effective power conversion under ambient environmental conditions, confirming its viability for supplying energy to low-power IoT sensor nodes. The proposed design achieves an effective compromise between compactness, wideband capability, and energy harvesting efficiency.

The evolution of wireless communication systems has led to the widespread use of low power electronic devices, particularly in applications such as the Internet of Things (IoT) and wireless sensor networks^{1,2}. The replacement of batteries in such devices is both time consuming and costly, and it carries an additional risk of environmental contamination resulting from improper disposal practices³. As a result, the increasing interest in harvesting ambient energy from multiple sources including solar power, wind flow, mechanical vibrations, heat differentials, and radio frequency (RF) emissions reflects its growing potential as a reliable solution for long term, sustainable power supply in low energy electronics⁴⁻⁶. RFEH distinguishes itself from other energy harvesting approaches by offering a reliable and sustainable power source, making it a compelling solution for long term energy needs. The continued evolution of wireless communication systems has resulted in a growing density of ambient RF signals originating from sources such as cellular infrastructure and wireless local area networks (WLANs),⁷⁻⁹. This surge in available RF energy has improved the viability of RF energy harvesting as an alternative means of powering low power electronic devices,^{10,11}.

In practical implementations involving continuously operating sensors, RFEH serves as an important mechanism for transforming incident EM waves into usable electrical power¹²⁻¹⁴. Although Wi-Fi at 2.45 GHz remains the dominant RF in indoor environments^{15,16}. Ambient RF energy is also abundantly available across a wide spectrum of frequency bands. These include LTE at 600 and 700 MHz, CDMA at 800 MHz, GSM at 900 MHz, GSM/4G at 1800 MHz, and signals from the Digital Terrestrial Television (DTT) band, making such energy accessible in both indoor and outdoor scenarios¹⁷. The insight presented herein originates from a thorough investigation of documented power spectrum analyses and empirical measurement findings in existing literature, where the performance and viability of multiple frequency bands were examined under both indoor and outdoor propagation conditions^{18,19}. Energy harvesting circuits are essential for delivering sufficient electrical power to support the operation of low power devices within IoT networks^{7,8}.

The antenna serves as a fundamental component in RFEH and WPTs, where it is responsible for efficiently transmitting and receiving RF signals essential for power conversion and delivery²⁰. The ambient environment is rich in RF signals exhibiting diverse polarization, which can be harnessed as a viable energy source for the operation of self powered devices without reliance on conventional batteries^{21,22}. In recent years, researchers have

¹Centre for Wireless Technology, CoE for Intelligent Network, Faculty of Artificial Intelligence and Engineering, Multimedia University, Persiaran Multimedia, 63100 Cyberjaya, Selangor, Malaysia. ²Center for Intelligent Network Telekom Research & Development (TM R&D), Sdn Bhd, Multimedia University, TM Innovation Centre, Lingkaran Teknokrat Timur, 63000 Cyberjaya, Selangor, Malaysia. ³College of Engineering, Al Ain University, 64141 Al Ain, UAE. ⁴Institut National de la Recherche Scientifique (INRS), Montreal H5A 1K6, QC, Canada. ✉email: usmanyau7@gmail.com; jjtiang@mmu.edu.my; aiqbal@ieee.org

increasingly concentrated on designing wideband antennas equipped with selective band rejection functionalities, aimed at mitigating interference caused by coexisting narrowband signals in modern wireless applications²³. Exhibiting a wideband characteristic provides a significant advantage in ambient RFEH applications, allowing the antenna to function across various prevalent RF frequency bands and thereby improving its ability to capture and accumulate adequate energy⁵. In pursuit of the targeted performance metrics, multiple design modifications have been employed, including the introduction of slits and slots of varying dimensions across the radiating structure, the feed line, and the ground plane, to enhance EM behavior and improve antenna characteristics^{24–26}. The use of $\lambda/2$ and $\lambda/4$ open-ended slit configurations^{8,12}, in conjunction with defected ground structures (DGS)^{27,28}, has been explored in the literature for enhancing performance across various wireless communication systems. In²⁹, the researchers developed a circular monopole antenna incorporating an annular-ring structure, specifically designed to function efficiently at a center frequency of 5.80 GHz. Compared to a typical monopole antenna, the presented design exhibits a 12.8% enhancement in BW and delivers a realized gain of 5.70 dBi at a comparatively higher operating frequency, thereby demonstrating improved performance characteristics suitable for high frequency applications. This paper³⁰ introduces the design and fabrication of a compact, printed wide-slot antenna incorporating a modified L-shaped microstrip feed line, tailored to support broadband wireless communication systems. The proposed antenna structure is realized on an FR-4 dielectric substrate characterized by a relative permittivity of 4.4. It demonstrates a broad BW of 3.51 GHz, spanning frequencies between 1.21 GHz and 4.72 GHz. Proposed³¹ an innovative back-to-back microstrip antenna configuration that integrates broadband omnidirectional wireless energy harvesting (2.03–4.08 GHz) with high-directivity WPT at 5.8 GHz, all within a compact design. The antenna demonstrated a measured BW exceeding 67%, and its harvesting performance remained consistent at incidence angles up to $\pm 60^\circ$, indicating strong angular robustness. Nevertheless, the study reported limitations including low harvested power levels and limited characterization of the radiation pattern at 5.8 GHz. In this work³², the authors introduced a compact coplanar waveguide (CPW)-fed bow-tie slot antenna designed to support wideband operation for IoT-integrated smart healthcare applications. The antenna is optimized to perform efficiently across the 1.41–1.86 GHz, which plays a vital role in enabling reliable WPT in IoT Sensor nodes. An improved broadband circularly polarized (CP) antenna was introduced in³³, featuring a DGS and a uniquely shaped radiating patch. The design enhances axial ratio BW and impedance matching across a broad frequency spectrum while maintaining a compact form factor without degrading performance. The fabricated antenna underwent experimental validation, exhibiting a broad axial ratio BW of approximately 81.5% across the frequency range. A peak gain of 4.2 dBi was recorded, and the antenna preserved consistent radiation characteristics throughout the entire operating band. In³⁴, the researchers introduced a compact multiband slot antenna designed specifically for wireless communication applications, covering GPS at 1.575 GHz, WiMAX at 2.4/3.5 GHz, and WLAN at 5.2/5.8 GHz. The antenna structure features a modified rectangular slot integrated into a microstrip-fed ground plane. To improve impedance matching and frequency selectivity, a T-shaped radiating stub is incorporated into the design, contributing to enhanced performance across the targeted frequency bands. Despite the antenna's capability to operate across multiple frequency bands with a compact form factor, the relatively low gain observed in specific bands may hinder its performance in scenarios that require robust signal propagation. This study³⁵, presents a CPW fed monopole antenna fabricated on an FR4 substrate, exhibiting quad-band resonance at essential wireless communication frequencies. The key contribution lies in the integration of multiple frequency bands within a single radiating structure, without any increase in the overall antenna footprint. Nevertheless, the Antenna exhibits limited BW at some resonant frequencies.

Numerous reported antenna designs suffer from inadequate impedance BW, preventing effective coverage of multiple RF sources. Additionally, many of these antennas demonstrate restricted gain and reduced efficiency when evaluated under practical deployment conditions. In addition, the lack of effective structural optimization has contributed to diminished power conversion performance, especially under operating conditions where multiple interfering signals are present. In order to mitigate the existing limitations observed in previous designs, this research work introduces an approach that enables wideband performance in a highly compact configuration, thereby addressing the fundamental limitations of conventional slot antennas, which typically require a compromise between achievable BW and antenna miniaturization. In the proposed design, an inverted T-shaped stub and a pair of E-shaped stubs are integrated into a rectangular slot, a configuration that supports wideband performance while simultaneously improving the uniformity and strength of the surface current distribution. This structural modification markedly improves impedance matching and operational BW while preserving the original physical footprint of the design. Furthermore, the antenna was experimentally characterized in an anechoic chamber and subsequently integrated with a rectifier circuit, thereby validating its practical feasibility for ambient RFEH in IoT sensor network applications. The main contributions are summarized as follows:

- (1) Wideband performance: The proposed antenna achieves a measured impedance BW of 1.05 GHz (0.84–1.89 GHz) and a peak realized gain of 4.86 dBi, offering superior size-to-performance ratio compared to existing designs.
- (2) Compact structure: The antenna maintains a compact footprint of $0.65\lambda_g \times 0.49\lambda_g$, making it suitable for integration in space constrained IoT and RFEH applications.
- (3) Innovative design approach: The integration of an inverted T-shaped stub and dual E-shaped stubs within a rectangular slot introduces multiple resonant modes and enhances surface current distribution, significantly improving impedance matching and BW.
- (4) Experimental validation: The proposed design was fabricated and experimentally validated in an anechoic chamber, demonstrating strong agreement between simulated and measured results

- (5) Energy harvesting integration: The antenna was successfully integrated with a rectifier circuit, confirming its capability for ambient RFEH under realistic conditions.

Antenna design and analysis

The geometry of the proposed wideband slot antenna is illustrated in Fig. 1. It features a rectangular slot measuring $68 \text{ mm} \times 44 \text{ mm}$ etched on one surface of the dielectric substrate. The slot is modified by incorporating an inverted T-shaped stub along its upper edge, accompanied by two E-shaped stubs positioned on the left-hand (LH) and right-hand (RH) sides of the slot. To achieve a compact footprint, the inverted T-shaped stub incorporates horizontal strips folded symmetrically on both ends. The rectangular slot is excited using a T-shaped feed patch, while the microstrip line is positioned on the opposite side of the substrate to facilitate effective coupling. The feed line is designed with a width of $W_f = 1.6 \text{ mm}$ to maintain a characteristic impedance of 50Ω . The feed line is symmetrically positioned on a large ground plane, which may obstruct the integration of additional electronic components on the printed circuit board (PCB). Alternatively, the feed line can be designed with a 90° bend or placed asymmetrically along the ground plane, thereby creating additional space for the placement of other circuit components. As most existing designs position the feed lines symmetrically on the ground plane for consistency and ease of comparison^{36–38}, our design adopts a similar configuration by placing the feed line symmetrically as well. To enhance impedance matching, a step is introduced on the lower section of the T-shaped feed patch at both the LHS and RHS. The proposed antenna achieves a wide impedance BW at the targeted f_o , making it suitable for efficient RFEH applications. This antenna design utilizes an FR-4 substrate,

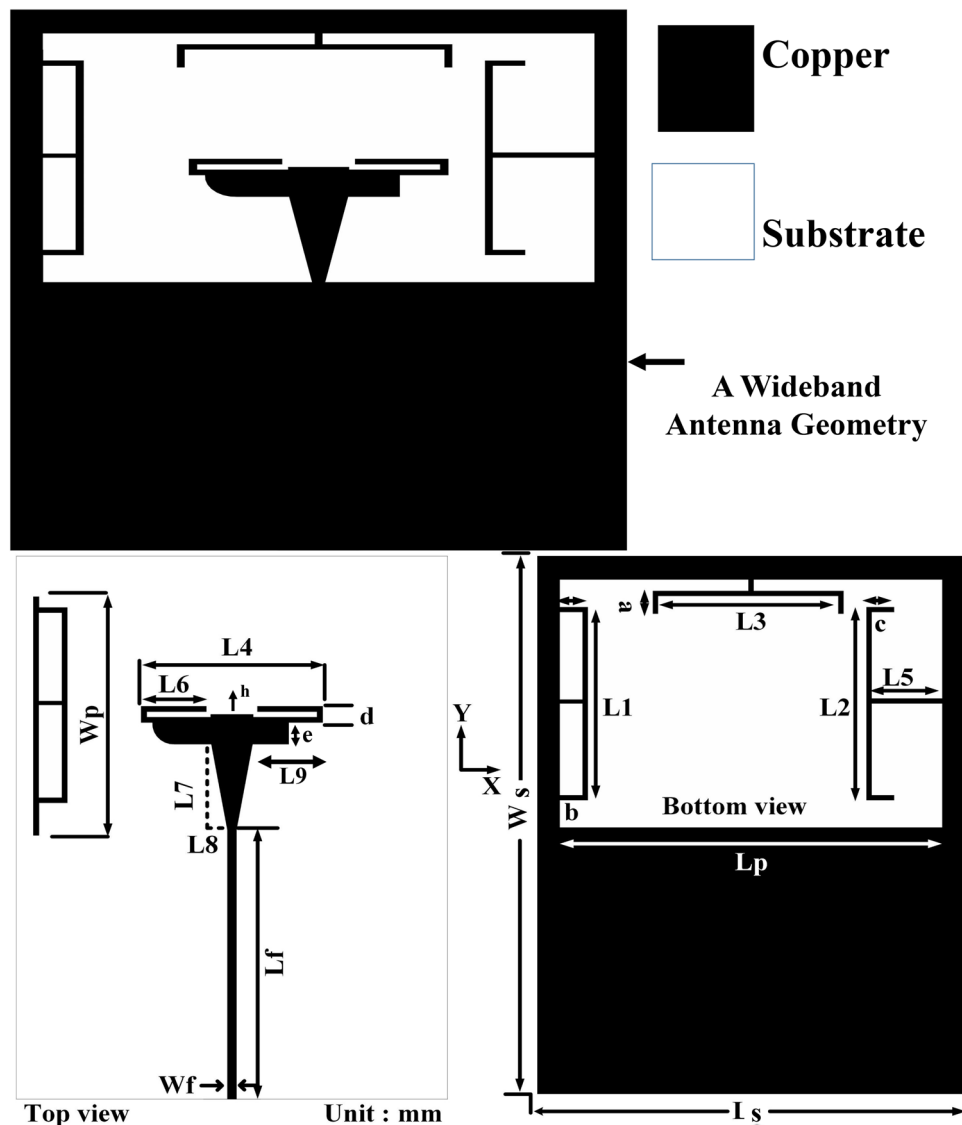


Fig. 1. Complete view of the wideband slot antenna. The parameters were systematically optimized according to the values outlined below: $L_s = 76$, $L_p = 68$, $L_1 = L_2 = 36$, $L_3 = L_4 = 32$, $L_5 = 12.5$, $L_6 = 11.5$, $L_7 = 15.4$, $L_8 = 2.83$, $L_9 = 12$, $L_f = 49.6$, $W_f = 1.6$, $W_p = 44$, $W_s = 100$, $a = 4.3$, $b = 5$, $c = 4$, $d = 3$, $e = 4$, $h = 1$: (All units are in mm).

which exhibits a dielectric constant $\epsilon_r = 4.4$, and a loss tangent of 0.02. The EM characteristics of the substrate were systematically evaluated and accounted for throughout the simulation and fabrication processes. The final dimensions of the proposed wideband antenna, utilized for fabrication of the prototype is depicted in Fig. 1, which was subsequently used for measurement.

The geometry of the design results from transforming a rectangular patch into four different configurations. The first configuration included only the T-shaped feed patch, the second added E-shaped stub to the LHS of feed followed by integrating inverted T-shaped stub and finally, the fourth scenario combined all elements into a complete structure. These were labeled as Ant-I, Ant-II, Ant-III, and the Proposed Antenna, respectively as shown in Fig. 2.

The results confirmed that the integrated contribution of each design element plays an important role in achieving the observed wideband characteristics. In the configuration of Ant-I, where only the T-shaped feed patch is embedded within the slot, the antenna exhibits limited impedance matching across a narrow frequency band. This constrained resonant response highlights inadequate EM coupling, thereby restricting its capability for wideband operation. The integration of an E-shaped stub in Ant-II led to a significant improvement in impedance matching and a noticeable extension of the operational BW. This enhancement is primarily attributed to the increased surface current distribution along the slot edges. Compared to Ant-I, Ant-II demonstrates deeper nulls and wider frequency coverage, suggesting the onset of resonant mode merging. When the inverted T-shaped stub is employed in Ant-III, the antenna exhibits a significantly enhanced BW performance. An enhanced impedance match is observed in the mid-frequency range, thereby extending the region where the reflection coefficient remains below -10 dB. The proposed configuration exhibits enhanced surface current distribution and introduces supplementary resonant modes, thereby facilitating a smoother transition between operating states. The proposed antenna, incorporating a rectangular slot, an inverted T-shaped stub, dual E-shaped stubs, and an extended T-feed patch, exhibits superior wideband performance through the synergistic integration of its structural elements. The measured reflection coefficient S_{11} remains consistently below -10 dB across the frequency range.

A thorough parametric analysis was carried out using HFSS. The return loss was evaluated across three structural variants: L_1 , L_3 , and L_5 . It was observed that the integration of these structural components substantially broadens the antenna's impedance BW, mainly as a result of multiple resonant pathways and effective mode coupling^{39,40}. Figure 3 demonstrates that varying L_1 within the range of 31–36 mm leads to a noticeable reduction in the lower resonance frequency. This phenomenon supports classical slot antenna behavior, where a longer slot effectively elongates the current path, thus decreasing the natural resonance. An empirical expression describing this variation in the lower resonant mode is given as:

$$f_1 = \frac{c}{2\ell_{\text{eq}}(\epsilon_{\text{eff}})^{1/2}}, \quad \text{where } \ell_{\text{eq}} = L + W \quad (1)$$

Here, ϵ_{eff} represents the effective dielectric constant, which is approximated as $\epsilon_{\text{eff}} = (\epsilon_r + 1)/2$, where ϵ_r denotes the relative permittivity of the substrate⁴¹. The parameter c indicates the speed of light in free space, while L and W correspond to the length and width of the rectangular slot, respectively. Due to its strong impact on the resonant frequency f_1 , the length L_1 plays a key role in setting the antenna's lower frequency boundary. When L_1 is tuned to 36 mm, the impedance matching noticeably improves, starting from 0.84 GHz. Also, from the equation:

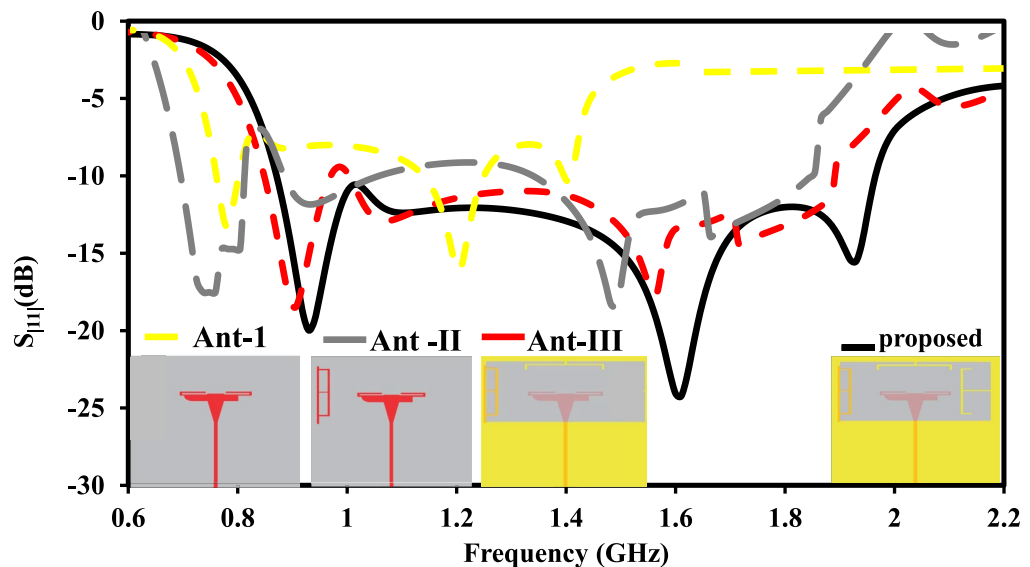


Fig. 2. A structured design methodology of the proposed wideband antenna.

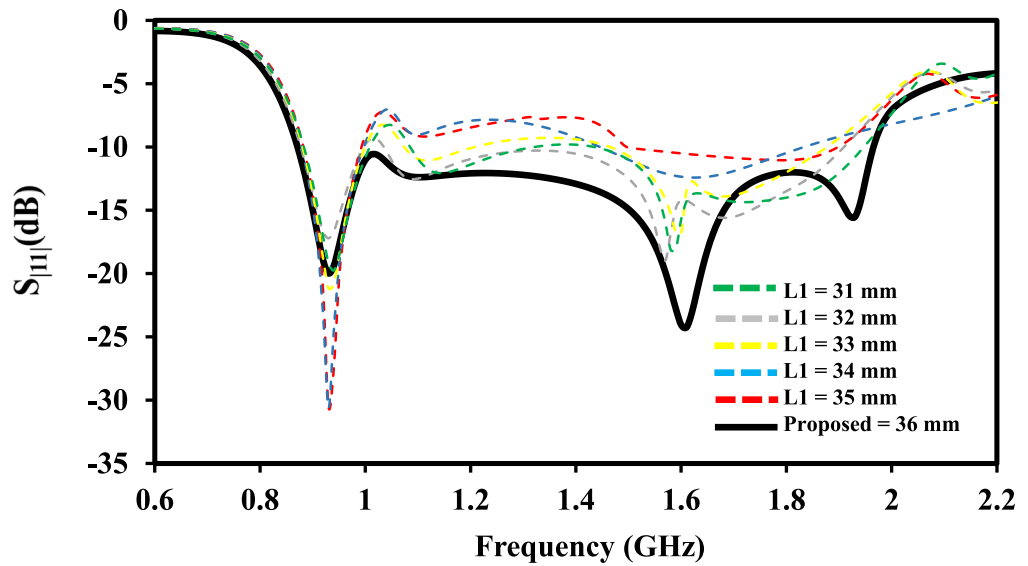


Fig. 3. Parametric analysis on L_1 .

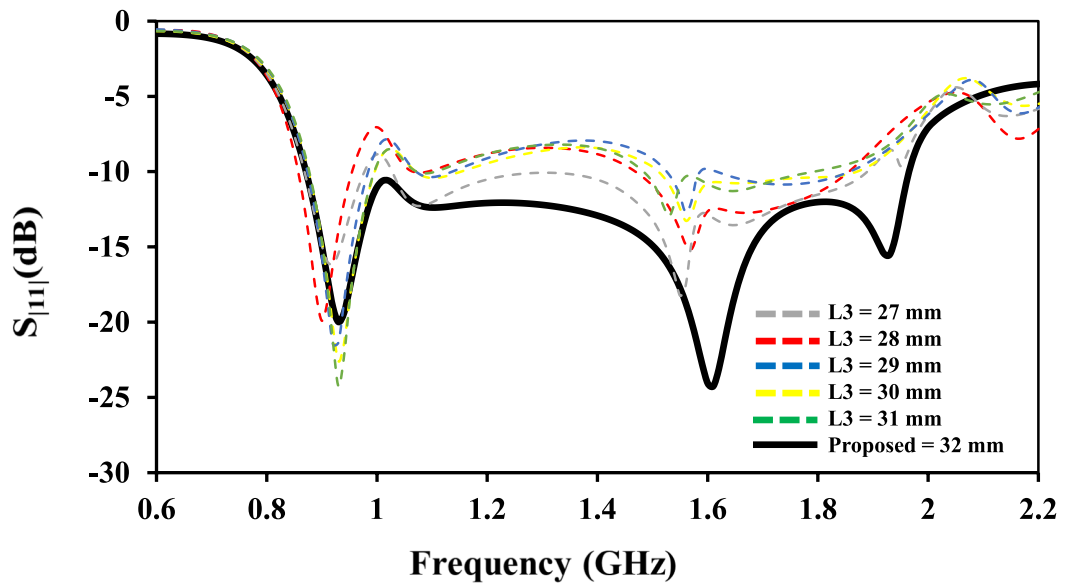


Fig. 4. Parametric analysis on L_3 .

$$\lambda_g = \frac{c}{f\sqrt{\epsilon_{eff}}} \tag{2}$$

The guided wavelength is used for the calculation of the length L_1 . Increase in the effective length lowered the resonance while decreasing L_1 raises it. In an optimally designed wide slot, the length L_1 is calculated as:

$$L_1 = \frac{\lambda_g}{2} = 36mm \tag{3}$$

Figure 4 illustrates the influence of varying L_3 , which corresponds to the vertical section of the inverted T-stub. Increasing L_3 extends the effective electrical length that supports the first higher-order slot resonance, causing a shift of this mode toward lower frequencies and promoting stronger coupling with the fundamental mode generated by the main rectangular slot. As a result, the interaction between these modes produces a wider continuous - 10 dB impedance BW. An increase in L_3 from 27 to 32 mm leads to a notable improvement in impedance BW and a reduction in return loss. The influence of L_3 on resonant mode convergence highlights its contribution to achieving a broader impedance BW, aligning with widely adopted principles in wideband antenna

design. In terms of equivalent circuit interpretation, the extended L_3 increases the shunt susceptible component near the feed slot interface, which facilitates improved real-part impedance matching across the mid-band frequencies, in conjunction with the contribution of the E-shaped stubs. Figure 5 demonstrates that modifying L_5 induces minor changes in the high-frequency band of the system's response. Although the modifications appear minimal, they clearly indicate that the E-shaped stubs function as auxiliary resonators, significantly affecting the mid-to-upper frequency band transitions. This observation aligns with the experimental results presented in³⁴, where the inclusion of E-shaped stubs was shown to improve resonance consistency across adjacent bands. The dual E-shaped stubs function as auxiliary quarter wavelength $\lambda/4$ resonators that introduce additional current paths along the vertical arms of the structure. These paths facilitate the merging of adjacent resonant modes, thereby smoothing the S_{11} response between resonances and flattening the impedance transition across the mid to upper frequency bands. Collectively, these effects result in a significant enhancement of the -10 dB impedance BW while maintaining a compact physical footprint. This behavior is consistent with the surface current redistribution observed in Fig. 13, particularly at 1.6 GHz, where strong current concentrations appear on the E-shaped stubs. Furthermore, the observed mid-band performance improvement aligns with the L_5 parametric sweep, which effectively adjusts the electrical length of the E-stubs, as illustrated in Fig. 4. The vertical portion of the E-stub is the dominant length setting this resonance express as:

$$f_2 = \frac{c}{4L_{stub}\sqrt{\epsilon_{eff}}} \quad (4)$$

where L_{stub} is the effective length of the E-shaped stub.

Simulation and experimental verified results

Figure 6 illustrates the measured and simulated reflection coefficient $|S_{11}|$ of the proposed wideband slot antenna across the operating frequency range. Both results remained within the acceptable limits of the target operating BW. The slight deviation observed in the measured response can be attributed to several factors, including misalignment during fabrication between the top and bottom layers, insertion loss associated with the SMA connector or feed cable, and signal degradation caused by soldering lead resistance. The proposed design exhibits a simulated impedance BW of 1.10 GHz ranging from 0.87 to 1.97 GHz, while the measured BW is 1.05 GHz spanning from 0.84 to 1.89 GHz, both defined at the -10 dB. The results demonstrate that the target resonant frequency, f_o , was achieved with a simulated and measured FBW of 77.5% and 77% respectively. Additionally, the measured $|S_{11}|$ response closely aligns with the simulated data, indicating good agreement between measured and simulated performance. At 1.9 GHz, the antenna achieves a peak realized gain of 4.97 dBi under simulation and 4.86 dBi based on measured results, as presented in Fig. 7.

The antenna's performance was evaluated through experimental measurements conducted in a fully lined anechoic chamber, ensuring minimal EM interference and signal reflection. As shown in Fig. 8, the antenna under test (AUT) was vertically mounted on a low profile, non-metallic tripod positioned at the center of a wooden turntable to maintain consistent rotational alignment. The measurement setup facilitated azimuthal rotation, thereby enabling a complete characterization of the far-field radiation pattern. A standard gain horn antenna was strategically placed at a suitable distance to function as the transmitting source, with both antennas properly aligned within the far-field region. The walls of the chamber were carefully lined with pyramidal RF

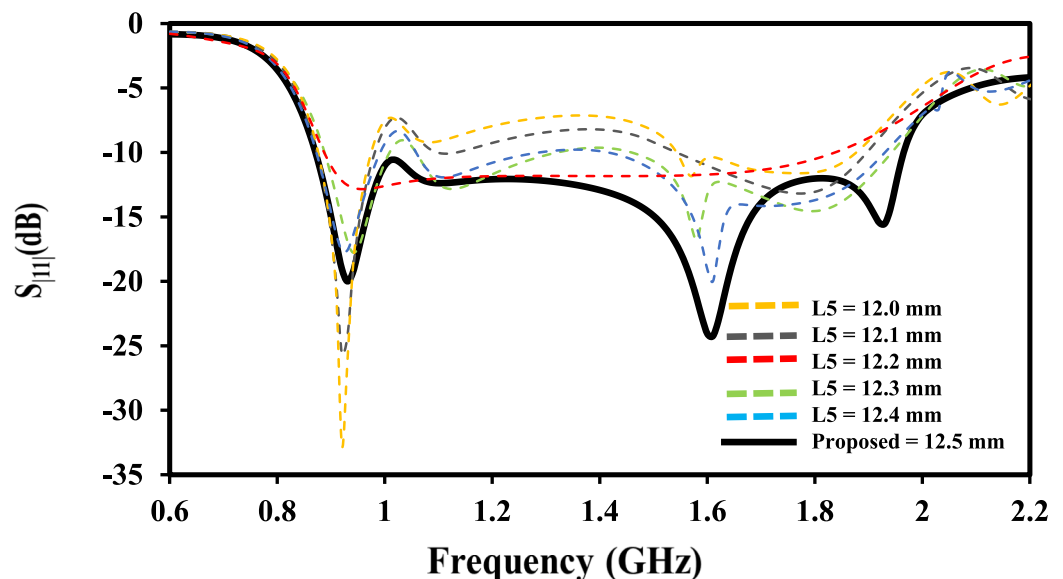


Fig. 5. Parametric analysis on L_5 .

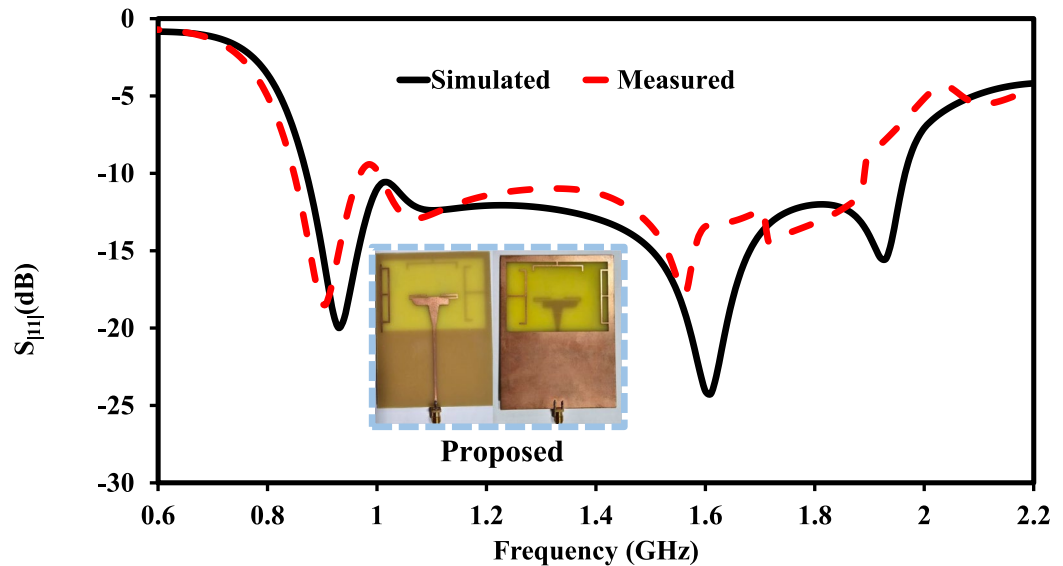


Fig. 6. Simulated and measured: reflection coefficient ($|S_{11}|$) of the Antenna as a function of frequency.

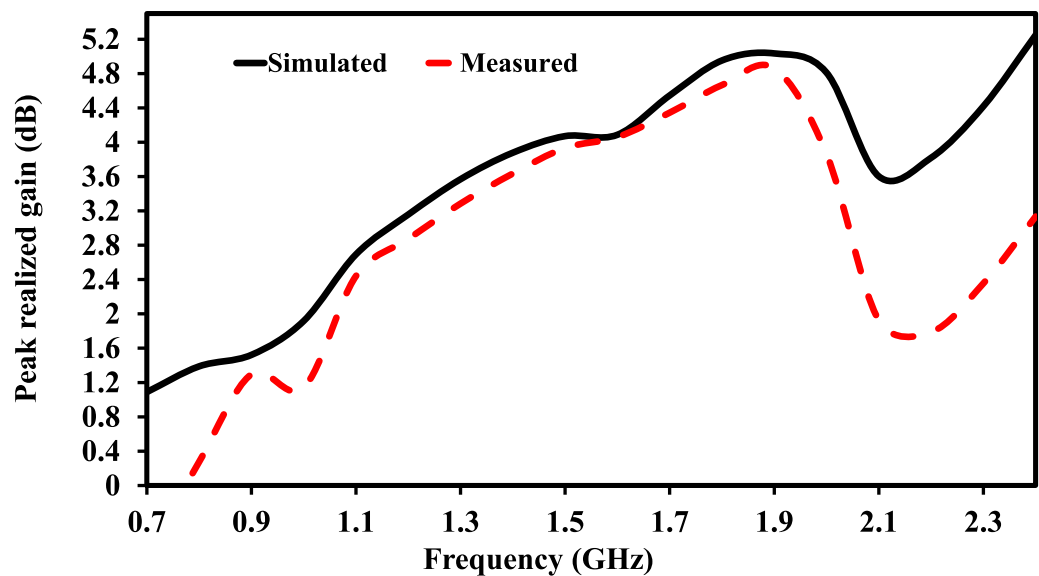


Fig. 7. Simulated and measured: peak realized gain, of the antenna as a function of frequency.

absorbents to simulate conditions similar to a free space environment, thereby minimizing EM reflections during measurements.

The radiation pattern corresponding to frequencies of 0.9, 1.47, 1.6, and 1.9 GHz are measured in both E and H plane as shown in Fig. 9. The comparison between measured and simulated results reveals a close agreement, exhibiting only minimal variations that are within acceptable limits. Across its designated operating frequency range, the proposed antenna achieves a favorable front-to-back (F/B) ratio, indicating effective directional radiation performance. At 0.9 GHz, the simulated E-plane radiation pattern exhibits a dominant main lobe oriented at 0° , achieving a peak gain of approximately 2.2 dBi. In contrast, the back lobe observed near 180° is suppressed to about -10 dBi, yielding a F/B ratio of approximately 12.2 dB. At the same operating frequency, the H-plane radiation pattern exhibits a main lobe gain of approximately 2 dBi, while the back lobe level is around -8 dBi. Consequently, the resulting F/B ratio is estimated to be about 10 dB. At 1.6 GHz, a marked enhancement in antenna performance is observed. The E-plane radiation pattern exhibits a forward gain of approximately 2 dBi, whereas the back lobe level is reduced to about -12 dBi, resulting in a F/B of 14 dB. The behavior in H-plane follows a comparable pattern, achieving a F/B ratio greater than 13 dB. These results demonstrate that the antenna retains acceptable directional discrimination performance, even at the lower boundary of the operating frequency band.

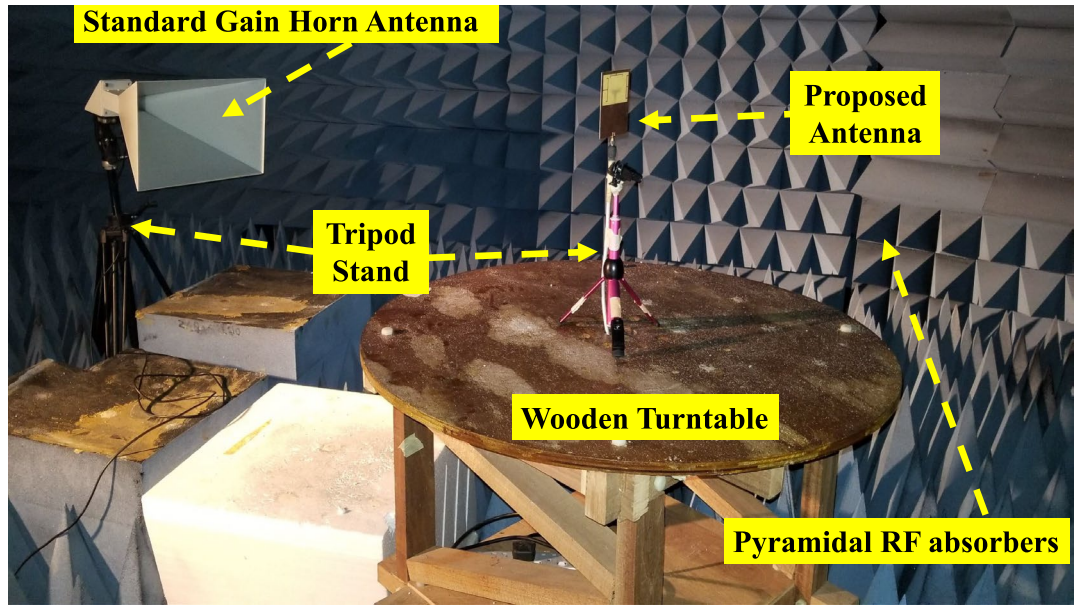


Fig. 8. Experimental setup for validating the performance of the antenna with a Horn Antenna in an anechoic chamber.

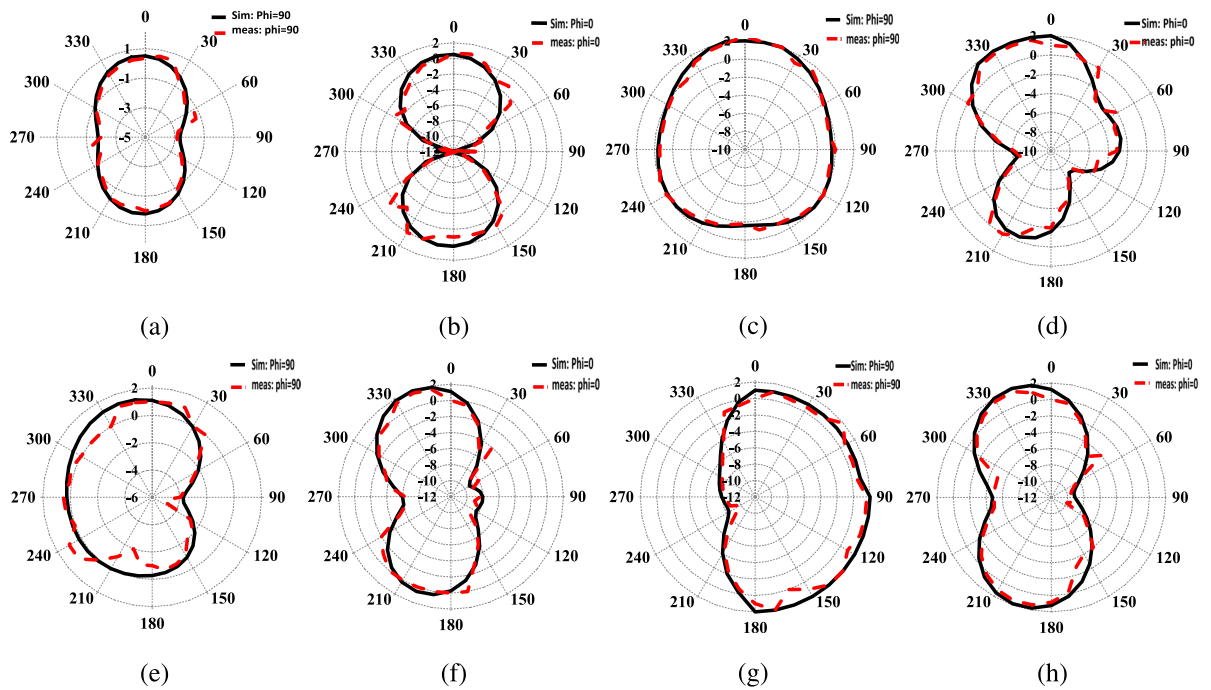


Fig. 9. Measured and simulated radiation patterns of the antenna for $\Phi = 0^\circ$ and $\Phi = 90^\circ$. (a, b) at 0.9 GHz; (c, d) at 1.47 GHz; (e, f) at 1.6 GHz; (g, h) at 1.9 GHz.

In order to assess the practical performance of the proposed RFEH system, a fully integrated rectenna was developed and subjected to experimental evaluation under real world ambient conditions. As shown in Fig. 10, the measurement setup comprised the antenna, a rectifier circuit, an RF spectrum analyzer and a digital multimeter. The antenna structure was precisely designed to enhance the efficient capture of incident EM energy. To enable the conversion of the received RF signals into a practical DC output, the antenna was integrated with a high-performance rectification circuit. The RF rectifier, previously subjected to extensive testing and validation as reported in⁴², demonstrates low insertion loss and is well-matched to the antenna’s operational frequency bands. The configuration of the rectifier circuit is illustrated in Fig. 11. Integrating this rectifier within the system enables a direct evaluation of the antenna’s real time energy harvesting performance under realistic



Fig. 10. Measurement setup for RFEH validation of the proposed antenna.

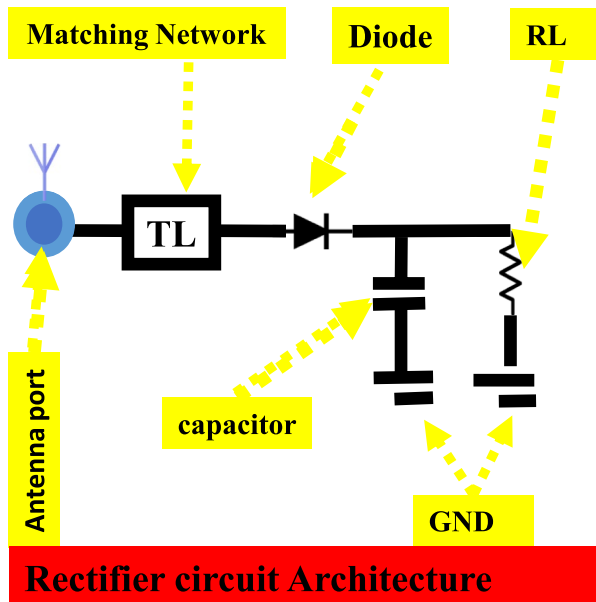


Fig. 11. Integrated RF-rectifier circuit layout.

environmental conditions. A Power Management Module (PMM) was later integrated to regulate and store the DC output harvested from the rectifier. Additionally, the PMM maintains voltage stability and facilitates continuous power delivery to connected IoT sensor nodes. Furthermore, the system incorporates a precise method for monitoring the extracted power, enabling a detailed evaluation of its energy harvesting efficiency. To characterize the ambient RF environment, a 6 GHz *Aim* spectrum analyzer (TTiPSA6005) was employed, facilitating real time observation of the incident spectral components. The DC output voltage generated by the system was concurrently measured using a DMM. Under typical ambient environmental conditions, the measured voltage was approximately 0.437 V. This result confirms the effective integration and performance of the antenna and rectifier system for ambient RFEH.

The antenna measurements and rectenna validation procedures were carried out under unbiased operating conditions, with no DC bias applied to the RF front end. The rectifier used employs a passive topology based on a Schottky diode and was characterized without the application of any external bias. Consequently, no biasing network was incorporated at the antenna input port. In systems where an active device is biased at the input, the associated biasing network may alter the input impedance matching, slightly affect radiation efficiency due to load variations, and necessitate the use of appropriate RF chokes and decoupling components to suppress unwanted coupling effects. Consequently, the results presented in this work characterize the antenna and rectenna performance under zero-bias operating conditions.

Figure 12 presents a comparison between the simulated and measured radiation efficiencies of the proposed antenna over the entire operating frequency range. The results indicate that the radiation efficiency remains largely consistent, with the measured values exhibiting close agreement with the simulated trend. A maximum efficiency of 86% is simulated and 84.5% measured at 2 GHz. Although small deviations are observed, particularly at higher frequency ranges, the measured differences remain within acceptable limits. These variations are primarily attributed to fabrication tolerances, connector related losses, and minor alignment inaccuracies introduced during the assembly process. The efficiency characteristics demonstrate that the antenna exhibits stable performance across the entire wideband operating region with, a feature that is essential for ensuring dependable RF energy harvesting. The simulated surface current distributions at 0.9 GHz, 1.47 GHz and 1.6 GHz, are shown in Fig. 13, providing insight into the antenna's current behavior across the operating band. At 0.9 GHz, the surface current is primarily distributed along the edges of the rectangular slot and the inverted T-shaped stub, which signifies effective EM coupling between the feeding structure and the radiating components. Also, at 1.6 GHz, the surface current distribution is predominantly concentrated on the E-shaped stubs, indicating that these elements play a significant role in exciting higher order resonant modes. The observed redistribution of surface currents among the various structural elements confirms the effectiveness of the proposed design methodology, in which multiple stubs are deliberately incorporated to realize wideband performance through efficient modal interaction and merging. Figure 14 presents the measured and simulated cross-polarization radiation patterns for both the E-plane and H-plane at 0.9 GHz and 1.6 GHz. At both operating frequencies, the antenna exhibits low cross-polarization levels, indicating that polarization purity is effectively maintained throughout the intended BW. This characteristic is critical for reducing signal degradation while enabling efficient energy capture under practical deployment conditions⁴³. Figure 15 shows the variation of RF-to-DC PCE with respect to P_{in} for the proposed wideband antenna integrated with the rectifier. To emulate practical operating scenarios of low-power IoT devices, the input power level was evaluated over a range extending from -30 dBm to 5 dBm. The results indicate a peak conversion efficiency of approximately 78.8%, achieved at an P_{in}

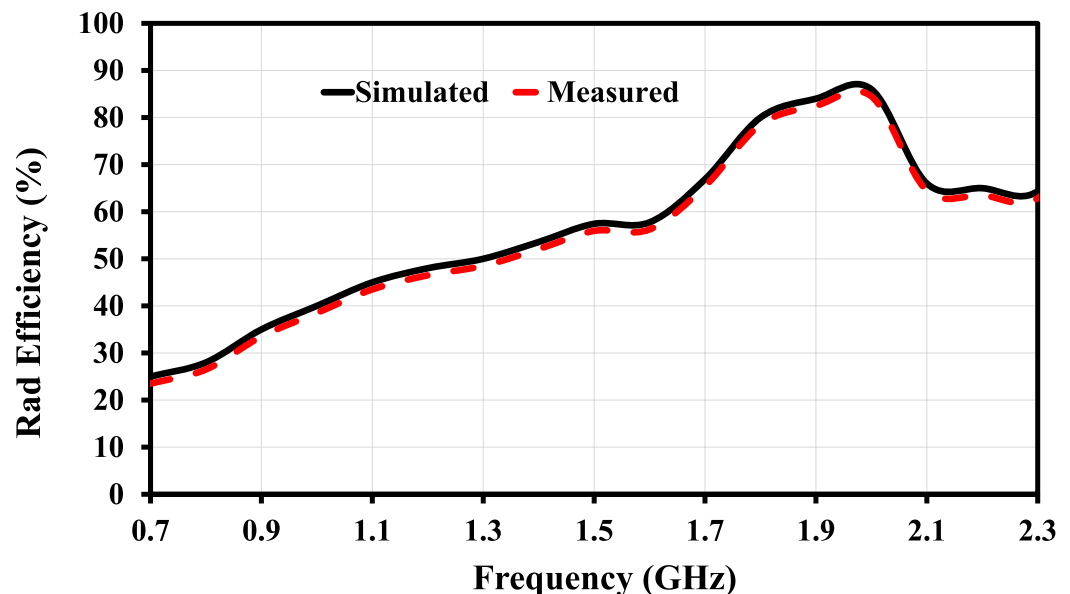


Fig. 12. Simulated and measured radiation efficiency of the antenna.

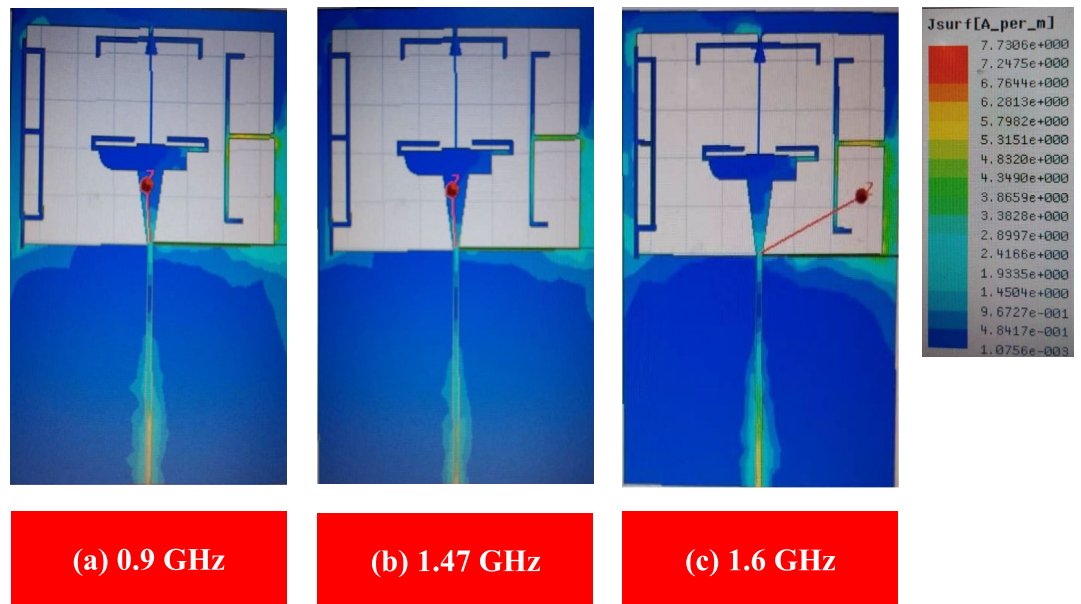


Fig. 13. Simulated surface current distribution of the antenna at (a) 0.9 GHz, (b) 1.47 GHz and (c) 1.6 GHz.

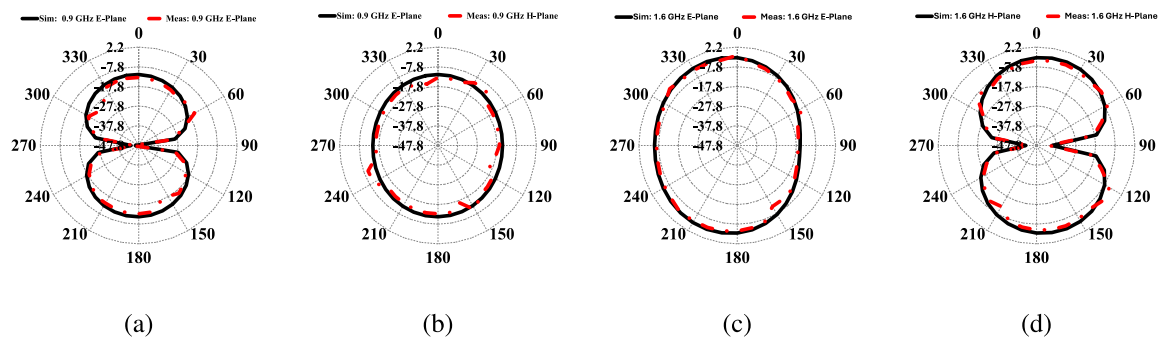


Fig. 14. Simulated and measured cross polarization patterns of the antenna for E and H planes: (a) Sim/Meas: 0.9 GHz E Plane; (b) Sim/Meas: 0.9 GHz H Plane; (c) Sim/Meas: 1.6 GHz E Plane; (d) Sim/Meas: 1.6 GHz H Plane.

of 4 dBm. The decrease in efficiency observed at lower input power levels is mainly attributed to the intrinsic threshold voltage characteristics of the diode.

A fabrication tolerance sweep of ± 0.1 mm on L_1 , L_3 , L_5 and ± 0.05 mm on W_f yields a frequency shift of $\leq \pm 20 - 30$ MHz for the lower resonance and a negligible impact on the upper band, while preserving an FBW of approximately 77% and the main beam profile, consistent with the measured and simulated.

Table 1 presents a comprehensive comparison between the proposed antenna and existing designs, considering dielectric substrate, impedance BW, peak gain, and normalized electrical dimensions. The proposed antenna demonstrates a measured impedance BW of 1.05 GHz, ranging from 0.84 GHz to 1.89 GHz, and achieves a peak realized gain of 4.86 dBi. The design maintains a compact form factor of $0.59\lambda_g \times 0.44\lambda_g$. While²⁹ and³⁴ exhibit commendable performance, they typically demand larger physical dimensions $2.7\lambda_g \times 1.7\lambda_g$ and $0.44\lambda_g \times 0.38\lambda_g$, designed on RO6002 and RO4003C respectively. In contrast, the proposed design shows significant reduced size. Moreover, the antenna presented in³⁰ provides an extended BW of 3.51 GHz, but poses relatively larger dimensions $1.12\lambda_g \times 1.66\lambda_g$. While designs in³¹ and³² offer compact footprints, they are constrained by limited BW, thereby limiting their applicability in high efficiency RFEH systems. In contrast to existing designs, the proposed antenna achieves a more favorable balance by maintaining compact dimensions while providing wideband operation and consistent gain performance.

Conclusion and future work

A novel wideband slot antenna is presented in this study, specifically designed to support RFEH for IoT sensor nodes. The integration of an inverted T-shaped stub along with dual E-shaped stubs within a rectangular slot configuration significantly improves the antenna's impedance BW and gain characteristics, while maintaining a compact physical profile. Extensive parametric optimization was conducted, and the performance was validated

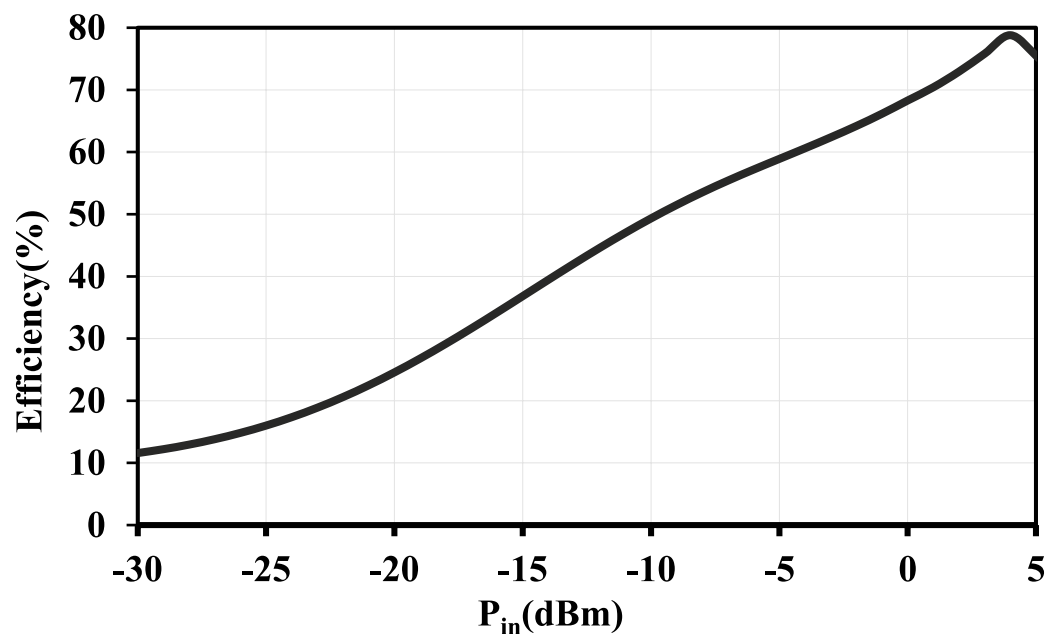


Fig. 15. Harvested DC power, PCE vs input power of the Rectenna.

Ref[...]	Relative permittivity (ϵ_r)	Bandwidth (GHz)	Peak gain (dBi)	Size ($\lambda_g \times \lambda_g$)	Radiation eff (%)	FBW (%)
This work	FR-4 (4.4)	(0.84–1.89), 1.05	4.86	0.59×0.44	86	77
²⁹	RO6002 (2.94)	(5.70–6.30), 0.60	5.70	2.70×1.70	75	10
³⁰	FR-4 (4.4)	(1.21–4.72), 3.51	4.10	1.12×1.66	70	118
³¹	F4B (4.4)	(2.03–4.08), 2.05	N/A	0.28×0.22	71.4	67
³²	FR-4 (4.4)	(1.41–1.86), 0.45	1.31	0.35×0.35	N/A	27.5
³³	FR-4 (4.4)	(1.60–3.80), 2.20	4.20	1.47×1.27	N/A	81
		(1.48–4.47), 2.99				100
³⁴	RO4003C (3.5)	(1.57–1.67), 0.09	5.50	0.44×0.38	76.8	5.5
		(2.40–2.54), 0.14				5.67
		(3.27–3.97), 0.70				19
		(5.17–5.93), 0.76				13.7
³⁵	FR-4 (4.4)	(2.62), 0.14	4.30	0.64×0.70	N/A	5.3
		(4.43), 0.11				2.48
		(5.37), 0.27				5.0
		(7.30), 0.37				5.06

Table 1. Performance evaluation of the proposed antenna compared to literature works. λ_g : Wavelength at the lowest operating frequency (f_o). N/A: Not Applicable.

through both numerical simulations and experimental measurements. The measured results demonstrate a wide impedance BW of 1.05 GHz and a peak gain of 4.86 dBi, exhibiting strong agreement with the simulated data. The integration of the antenna with a rectifier circuit resulted in effective power conversion efficiency in ambient RF environments, demonstrating its potential for practical deployment in ambient energy harvesting applications. The proposed antenna demonstrates an enhanced balance among physical size, operational BW, and radiation efficiency when compared to prior designs, thereby positioning it as a viable solution for sustainable energy delivery in IoT sensor nodes. Future research will focus on achieving further miniaturization and integrating adaptive power management systems to improve deployment flexibility and operational efficiency.

Data availability

All data generated or analysed during this study are included in this published article.

Received: 4 September 2025; Accepted: 18 February 2026

Published online: 25 February 2026

References

- Moloudian, G. et al. Rf energy harvesting techniques for battery-less wireless sensing, industry 4.0, and internet of things: a review. *IEEE Sens. J.* **24**, 5732–5745 (2024).
- Choudhary, V., Guha, P., Pau, G. & Mishra, S. An overview of smart agriculture using internet of things (iot) and web services. *Environ. Sustain. Indic.* **2025**, 100607 (2025).
- Phogat, P., Dey, S. & Wan, M. Powering the sustainable future: a review of emerging battery technologies and their environmental impact. *RSC Sustain.* **2025**, 256 (2025).
- Ibrahim, H. H. et al. Radio frequency energy harvesting technologies: a comprehensive review on designing, methodologies, and potential applications. *Sensors* **22**, 4144 (2022).
- Kumar, M., Suhaib, M., Sharma, N., Kumar, S. & Choudhary, S. Energy harvesting technologies in mechanical systems: a comprehensive review. *Int. J. Res. Publ. Rev.* **5**, 2782–2787 (2024).
- Zahari, M. et al. Powering the future of farming: Rf energy harvesting for environmental sustainability. *IOP Conf. Ser. Earth Environ. Sci.* **1397**, 012022 (2024).
- Safaei, B., Peiravian, M. & Siamaki, M. Eco-friendly iot: leveraging energy harvesting for a sustainable future. *IEEE Sens. Rev.* **2025**, 256 (2025).
- Boumaiz, M., Ghazi, M. E., Bouayad, A., Balboul, Y. & El Bekkali, M. Energy-efficient strategies in wireless body area networks: a comprehensive survey. *IoT* **6**, 49 (2025).
- Pahlavan, K. & Krishnamurthy, P. Evolution and impact of wi-fi technology and applications: a historical perspective. *Int. J. Wirel. Inf. Netw.* **28**, 3–19 (2021).
- Singh, S., Kumar, M. & Kumar, R. Powering the future: a survey of ambient rf-based communication systems for next-gen wireless networks. *IET Wirel. Sensor Syst.* **14**, 265–292 (2024).
- Ramalingam, L. et al. The advancement of radio frequency energy harvesters (rfehs) as a revolutionary approach for solving energy crisis in wireless communication devices: a review. *IEEE Access* **9**, 106107–106139 (2021).
- Soleimani, J. & Karabulut-Kurt, G. Comprehensive survey on design challenges. High-power radio frequency wireless energy transfer system. *IET Wirel. Sensor Syst.* **14**, 248–264 (2024).
- Arinze, S. N., Obi, E. R., Ebeonuwa, S. H. & Nwajana, A. O. Rf energy-harvesting techniques: applications, recent developments, challenges, and future opportunities. In *Telecom*, vol. 6 45 (MDPI, 2025).
- Mahenge, E., Sinde, R., Dida, M. A. & Sam, A. E. Radio frequency energy harvesting for underground sensor nodes: possibilities and challenges. *IEEE Access* **12**, 43772–43788 (2024).
- McKenzie, R. J., Iskra, S. & Knipe, P. Assessment of radio frequency fields in the 2.45 ghz band produced by smart home devices. *Bioelectromagnetics* **45**, 184–192 (2024).
- Dembélé, H. Characterization of wi-fi access point energy consumption and the impact of ieee 802.11 standard evolutions. *IEEE Access* (2025).
- Nadali, K., Maurya, N. K., McEvoy, P. & Ammann, M. J. A dual-band dual-polarized antenna for harvesting in cellular and digital terrestrial television bands. *IEEE Open J. Antennas Propag.* **5**, 1489–1498 (2024).
- Sheikh, M. U., Ruttik, K., Jäntti, R. & Hämäläinen, J. Analysis of radio propagation with different antenna solutions at sub-thz band in an indoor (tee-junction) environment using ray tracing simulations. *Telecommun. Syst.* **88**, 1–11 (2025).
- Faruk, N. et al. Large-scale radio propagation path loss measurements and predictions in the vhf and uhf bands. *Heliyon* **2021**, 7 (2021).
- Ullah, M. A. et al. A review on antenna technologies for ambient rf energy harvesting and wireless power transfer: Designs, challenges and applications. *IEEE Access* **10**, 17231–17267 (2022).
- Jiang, C. et al. Wireless technologies for energy harvesting and transmission for ambient self-powered systems. *ACS Nano* **15**, 9328–9354 (2021).
- Nwalike, E. D. et al. Harnessing energy for wearables: a review of radio frequency energy harvesting technologies. *Energies* **16**, 5711 (2023).
- Kumar, O. P., Kumar, P., Ali, T., Kumar, P. & Vincent, S. Ultrawideband antennas: growth and evolution. *Micromachines* **13**, 60 (2021).
- Sharma, N. & Bhatia, S. S. Stubs and slits loaded partial ground plane inspired hexagonal ring-shaped fractal antenna for multiband wireless applications: design and measurement. *Progress Electromagn. Res. C* **112**, 99–111 (2021).
- Anand, S. & Pavithran, K. Pin-switched series feed for frequency-and pattern-reconfigurable mimo antenna using merged srr, siw, and symmetric slit extensions. *Arab. J. Sci. Eng.* **2025**, 1–31 (2025).
- Reis, S., Silva, F., Albuquerque, D. & Pinho, P. General overview of antennas for unmanned aerial vehicles: a review. *Electronics* **14**, 3205 (2025).
- Fernández-Prieto, A. Defected ground structure (dgs) based antennas: design physics, engineering, and applications [book review]. *IEEE Antennas Propag. Mag.* **66**, 96–98 (2024).
- Suganya, E., Prabhu, T., Palanisamy, S. & Salau, A. O. Design and performance analysis of l-slotted mimo antenna with improved isolation using defected ground structure for s-band satellite application. *Int. J. Commun. Syst.* **37**, e5901 (2024).
- Behera, B. R. & Mishra, S. K. Investigation of a high-gain and broadband circularly polarized monopole antenna for rf energyharvesting application. *Int. J. Microw. Wirel. Technol.* **15**, 781–792 (2023).
- Sung, Y. A printed wide-slot antenna with a modified l-shaped microstrip line for wideband applications. *IEEE Trans. Antennas Propag.* **59**, 3918–3922 (2011).
- Zhang, P. et al. Back-to-back microstrip antenna design for broadband wide-angle rf energy harvesting and dedicated wireless power transfer. *IEEE access* **8**, 126868–126875 (2020).
- Dayo, Z. A. et al. A compact cpw-fed multiband bow-tie slot antenna for iot smart healthcare wireless communication applications. In *2022 IEEE 95th Vehicular Technology Conference (VTC2022-Spring)* 1–5 (IEEE, 2022).
- Lee, C.-H. & Chang, Y.-H. An improved design and implementation of a broadband circularly polarized antenna. *IEEE Trans. Antennas Propag.* **62**, 3343–3348 (2014).
- Cao, Y., Cheung, S. & Yuk, T. A multiband slot antenna for gps/wimax/wlan systems. *IEEE Trans. Antennas Propag.* **63**, 952–958 (2015).
- Donthireddy, P., Nenturi, R. R., Terupally, H. & Chilukuri, S. A cpw fed compact multiband antenna for wireless applications. In *2022 IEEE Wireless Antenna and Microwave Symposium (WAMS)* 1–5 (IEEE, 2022).
- Boujmil, N. et al. A wideband cpw-fed annular ring patch antenna design for sub-terahertz applications. In *2025 International Conference on Circuit, Systems and Communication (ICCS)* 1–6 (IEEE, 2025).
- Srinivas, M. et al. Design and fabrication development of slotted t-shaped patch antenna with symmetrical cpw feed for iot and itu applications. *Plasmonics* **20**, 4345–4354 (2025).
- Samal, P. B., Soh, P. J. & Zakaria, Z. Compact microstrip-based textile antenna for 802.15. 6 wban-uwb with full ground plane. *Int. J. Antennas Propag.* **2019**, 8283236 (2019).
- Khan, I. et al. A novel multiband low mutual coupling quad-element mimo antenna for advanced communication systems. *IEEE Access* (2025).
- Lin, J.-F. & Zhu, L. Bandwidth and gain enhancement of patch antenna based on coupling analysis of characteristic modes. *IEEE Trans. Antennas Propag.* **68**, 7275–7286 (2020).

41. Dawar, P., Raghava, N. & De, A. Uwb, miniaturized and directive metamaterial loaded antenna for satellite applications. *Int. J. Netw. Distrib. Comput.* **6**, 24–34 (2018).
42. Muhammad, S. et al. A multiband ssr diode rf rectifier with an improved frequency ratio for biomedical wireless applications. *Sci. Rep.* **13**, 13246 (2023).
43. Elias, F. et al. Design of multi-sourced mimo multiband hybrid wireless rf-perovskite photovoltaic energy harvesting subsystems for iots applications in smart cities. *Technologies* **13**, 92 (2025).

Acknowledgements

The authors acknowledge the support of TM Research and Development (TM R&D) Malaysia for this work, funded under the Academic Co-Creation Project (Grant No. RDTC/241135: WBT-BIOM) and Project MMUE/240100 (*Corresponding authors: Amjad Iqbal (aiqbal@ieee.org), Jun Jiat Tiang (jjtiang@mmu.edu.my), Usman Yau (usmanyau7@gmail.com)).

Author contributions

U.Y., J.J.T., S.M., N.K.M., and A.I. wrote the main manuscript text and prepared all figures. All authors reviewed the manuscript.

Competing interests

The authors declare no competing interests.

Additional information

Correspondence and requests for materials should be addressed to U.Y., J.J.T. or A.I.

Reprints and permissions information is available at www.nature.com/reprints.

Publisher's note Springer Nature remains neutral with regard to jurisdictional claims in published maps and institutional affiliations.

Open Access This article is licensed under a Creative Commons Attribution-NonCommercial-NoDerivatives 4.0 International License, which permits any non-commercial use, sharing, distribution and reproduction in any medium or format, as long as you give appropriate credit to the original author(s) and the source, provide a link to the Creative Commons licence, and indicate if you modified the licensed material. You do not have permission under this licence to share adapted material derived from this article or parts of it. The images or other third party material in this article are included in the article's Creative Commons licence, unless indicated otherwise in a credit line to the material. If material is not included in the article's Creative Commons licence and your intended use is not permitted by statutory regulation or exceeds the permitted use, you will need to obtain permission directly from the copyright holder. To view a copy of this licence, visit <http://creativecommons.org/licenses/by-nc-nd/4.0/>.

© The Author(s) 2026